ANNALS OF GEOPHYSICS, 66, 6, SE640, 2023; doi:10.4401/ag-8884
OPEN ACCESS

Schumann resonance anomalies associated with two (M~7) Tohoku offshore earthquakes in the spring of 2021

Masashi Hayakawa[*,1,2], Jun Izutsu[3], Alexander P. Nickolaenko[4], Alexander Schekotov[5], Yuriy P. Galuk[6], Irina G. Kudintseva[7]

(1) Hayakawa Institute of Seismo Electromagnetics Co. Ltd. (Hi-SEM), The University of Electro-Communications (UEC) Alliance Center #521, 1-1-1 Kojima-cho, Chofu, 182-0026, Japan

(2) UEC, Advanced Wireless and Communications Research Center (AWCC), 1-5-1 Chofugaoka, Chofu, 182-8585, Japan

(3) Chubu University, International Digital Earth Applied Science Research Center, 1200 Matsumoto-cho, Kasugai Aichi, 487-8585, Japan

(4) A.Ya. Usikov Institute for Radio-Physics and Electronics, National Academy of Sciences of Ukraine, Kharkov, Ukraine

(5) Institute of Physics of the Earth (IPE), Russian Academy of Sciences, 123995, 10 Bolshaya Gruzinskaya, Moscow, Russia

(6) Institute of Physics of the Earth (IPE), Russian Academy of Sciences, 123995, 10 Bolshaya Gruzinskaya, Moscow, Russia

(7) Department of Mathematics and Informatics, V.N. Karazin Kharkov State University, Kharkov, Ukraine

Article history: received July 28, 2022; accepted Jaunary 9, 2023

Abstract

We describe the Schumann resonance anomalies associated with two earthquakes observed in Japan in the spring of 2021. The natural source of ELF (extremely low frequency) radiation is the global lightning activity occurring in the Earth-ionosphere cavity. The anomalies as the enhancement of the fourth harmonic were observed for the first time in Japan for the earthquakes in Taiwan when the distance between the observatory and the epicenter was a few Mm (1 Mm = 1000 km). Recently, a new Schumann resonance anomaly was addressed, related to nearby (at the distance of a few hundred km) earthquakes. This paper presents the Schumann resonance anomalies observed in the vicinity of Nagoya-city for two relatively close (~500 km) successive earthquakes with magnitude around 7 that occurred offshore the Tohoku area in Japan. The anomaly is characterized by the noticeable simultaneous increase or decrease in the amplitudes of three modes. This Schumann resonance unusual behavior was observed prior to and after each of the two earthquakes that occurred in February and March, 2021. Observational data were interpreted in the model of seismogenic perturbations of the lower ionospheric conductivity profile. Model computations imply the full-wave solution of the ELF electromagnetic problem in the form of the Riccati equation and the two dimensional telegraph equations. We show that observed disturbances in the Schumann resonance power spectra might be attributed to two types of seismogenic modifications in the lower ionospheric profile: the compression or the expansion of the vertical profiles of mesospheric conductivity over the earthquake epicenter.

Keywords: ELF (extremely low frequency) spectra; Schumann resonance (SR) anomalies; Seismogenic mesospheric perturbations; Nearby earthquakes (EQs)

1. Introduction

A frontier science field of seismo-electromagnetics, i.e., electromagnetic phenomena associated with earthquakes (EQs) or mainly taking place before an EQ, for the sake of short-term EQ prediction has made an enormous progress during the last few decades [e.g., Pulinets and Boyarchuk, 2004; Molchanov and Hayakawa, 2008; Hayakawa (Ed), 2009, 2013; Surkov and Hayakawa, 2014; Hayakawa, 2015; Sorokin et al., 2015; Ouzounov et al. (Eds), 2018]. Especially, among many electromagnetic precursors, it is found that the ionosphere both in the lowest part and in the upper F region is very sensitive to pre-EQ lithospheric seismic activity [e.g., Hayakawa et al., 2010; Liu et al., 2006; Picozza et al., 2021; Conti et al., 2021], and it can be a promising candidate for short-term EQ prediction. However, the mechanism on why and how the ionosphere is reacting to the lithospheric activity during the EQ preparatory phase regarded as "Lithosphere-atmosphere-ionosphere coupling (LAIC)" [Molchanov et al., 2004], is not well understood even though a few possible channels have already been proposed [Molchanov and Hayakawa, 2008; Freund, 2013; Sorokin et al., 2015; De Santis et al., 2019: Sorokin et al., 2020; Lizunov et al., 2020]. So, this topic has been of current interest for the last ten years, and many scientists have been working on the elucidation of this LAIC process with the use of multi-parameter ground- and satellite-based observations [e.g., Ouzounov et al. (Eds), 2018; Sasmal et al., 2021; Hayakawa et al., 2021a].

On the other hand, being closely related to the LAIC process, natural electromagnetic emissions are another important core of seismo-electromagnetics. Recently, Hayakawa et al. [2019] have reviewed those naturally-occurring electromagnetic radiation in the frequency ranges of ULF (ultra low frequency), ELF (extremely low frequency) and VLF (very low frequency), and they have suggested the invaluable phenomena for short-term EQ prediction including ULF effects (lithospheric ULF radiation [e.g., Hayakawa et al., 2011], ULF depression as a signature of lower ionospheric perturbations [Schekotov et al., 2006, 2013], atmospheric ULF/ELF electromagnetic emissions [Schekotov et al., 2007, 2013, 2017], and Schumann resonance (SR) anomalies [see a review by Hayakawa et al. 2020a].

This paper deals with the last observational item of SR anomalies. SR is the global electromagnetic resonance of the Earth-ionosphere cavity driven by the world-wide lightning activity in the ELF band, and is the global electromagnetic resonance phenomenon, and its resonance peaks are observed in the power spectra on natural radio noise at frequencies of 8, 14, 20, Hz, etc. [Nickolaenko and Hayakawa, 2002, 2014; Nickolaenko et al., 2016a,b]. The first anomaly was found as an enhancement of SR of higher modes (3^{rd} or 4^{th}), as a case study, in the ELF data observed at Nakatsugawa station (NAK) of Chubu University ELF network (which will be explained later) in possible association (mainly before) with the huge Chi-Chi EQ in Taiwan [Hayakawa et al., 2005]. It was followed by a later statistical study at the same station for the EQs with the magnitude (M_{EQ}) exceeding 5.0 in Taiwan by Ohta et al. [2006, 2009]. Recently, this kind of SR anomaly has attracted a lot of attention by different workers in the world [Fidani, 2006; Ouyang et al., 2013; Zhou et al., 2013; Gazquez et al., 2017; Christofilakis et al., 2019; Figueredo et al., 2021; Florios et al., 2021; Tritakis et al., 2022]. Those works are mainly concerned with the cases of distant EQs with a few Mm from the observing station. Recently, Hayakawa et al. [2020a] addressed theoretically the expected SR anomalies from the nearby EQs. They have indicated the effect from nearby EQs as an enhancement of SR intensities arising from modulations of the local height gain coefficient. The present paper presents the additional observational evidence for this effect associated with two large EQs (magnitude M_{EQ}~7) in the Tohoku offshore in Japan in the spring of 2021with special reference to the differences in morphological characteristics of SR before and after each EQ. We try to interpret those results in terms of the changes in mesospheric conductivity before and after the EQ, to be compared with our latest paper [Hayakawa et al., 2021b]. These results support an old-days initial brief report by Maki and Ogawa [1983].

The structure of the paper is as follows. We first describe the measurement equipment and observational data; introduce the model of seismogenic modifications in the mesosphere above the EQ; present the computational data; compare the model diurnal variations with experiments; and finally discuss the results and make conclusions.

2. ULF/ELF observatories and EQ events

The magnetic field data have been obtained by the Chubu University ULF/ELF network consisting of three observatories: Shinojima (abbreviated as SHI, geographic coordinates 34.67° N, 137.01° E), Nakatsugawa (NAK, 35.42° N, 137.55° E) and Izu (IZU, 34.64° N, 138.85° E). At each station we observe three field components (B_x, B_y, and B_z components) with three orthogonal induction-type magnetometers in the frequency range of 0.1-50 Hz. The data are digitized with the sampling frequency of 100 Hz with the use of the 16-bit DAS, and stored on a hard disk. Those data are transmitted to the master station of the university at Kasugai. See the details of the equipment in Hata et al. [2010] and Ohta et al. [2013].

The IZU station was not working during the period of our interest, and so we use the data from SHI and NAK. But only the data from SHI cover the whole period from the beginning of January to the end of March, so that they will be presented below.

Spectra were collected during local night because of low level of industrial interference in the interval from 01 to 05 h JST (16-20 h UT). The Welch's technique was used for the spectral analysis [Welch, 1967], and individual spectra were computed using FFT with $N_{fft} = 512$ samples of sampling frequency, $f_s = 100$ Hz.

It seems that a significant enhancement takes place in the first quarter of 2021 in the seismic activity on the Pacific Ocean side of Japan Island. Probably, we observe the aftershocks of the disastrous 2011 Tohoku EQ. There happened two huge EQs in the Tohoku offshore in the beginning of 2021, which are:

1st EQ: 2021 February 13; 14:07 UT; epicenter at (37.7 N, 141.7 E); $M_{EQ} = 7.3$
2nd EQ: 2021 March 20; 09:09 UT; epicenter at (38.5 N, 141.6 E); $M_{EQ} = 6.9$

The EQ magnitude M is obtained from Japan Meteorological Agency. Fig. 1 illustrates the positions of these two EQs together with the ULF/ELF observatory of SHI and NAK, and the distances of those EQ epicenters from the observatory are about 500 km.

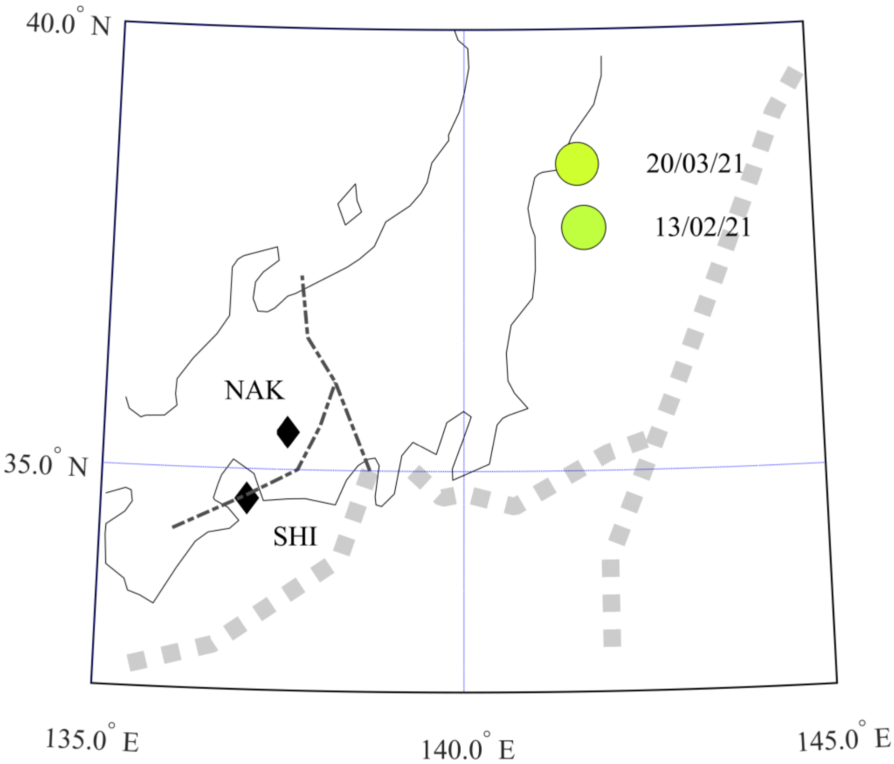

Figure 1. Location of two EQs of our interest (green circles) and positions of our ULF/ELF stations (NAK and SHI). Broken lines indicate the major faults in Japan Island and grey dotted lines refer to the Japanese trenches in the sea.

3. SR receiving system

All three observatories exploit similar standard equipment. This is essentially the three component magnetometer designed for working in the ULF/ELF bands. The time synchronization of analogue to digital convertors (ADCs) with the help of GPS time stamps of 1 s discretization allows us to obtain the digital records performed simultaneously a)

b)

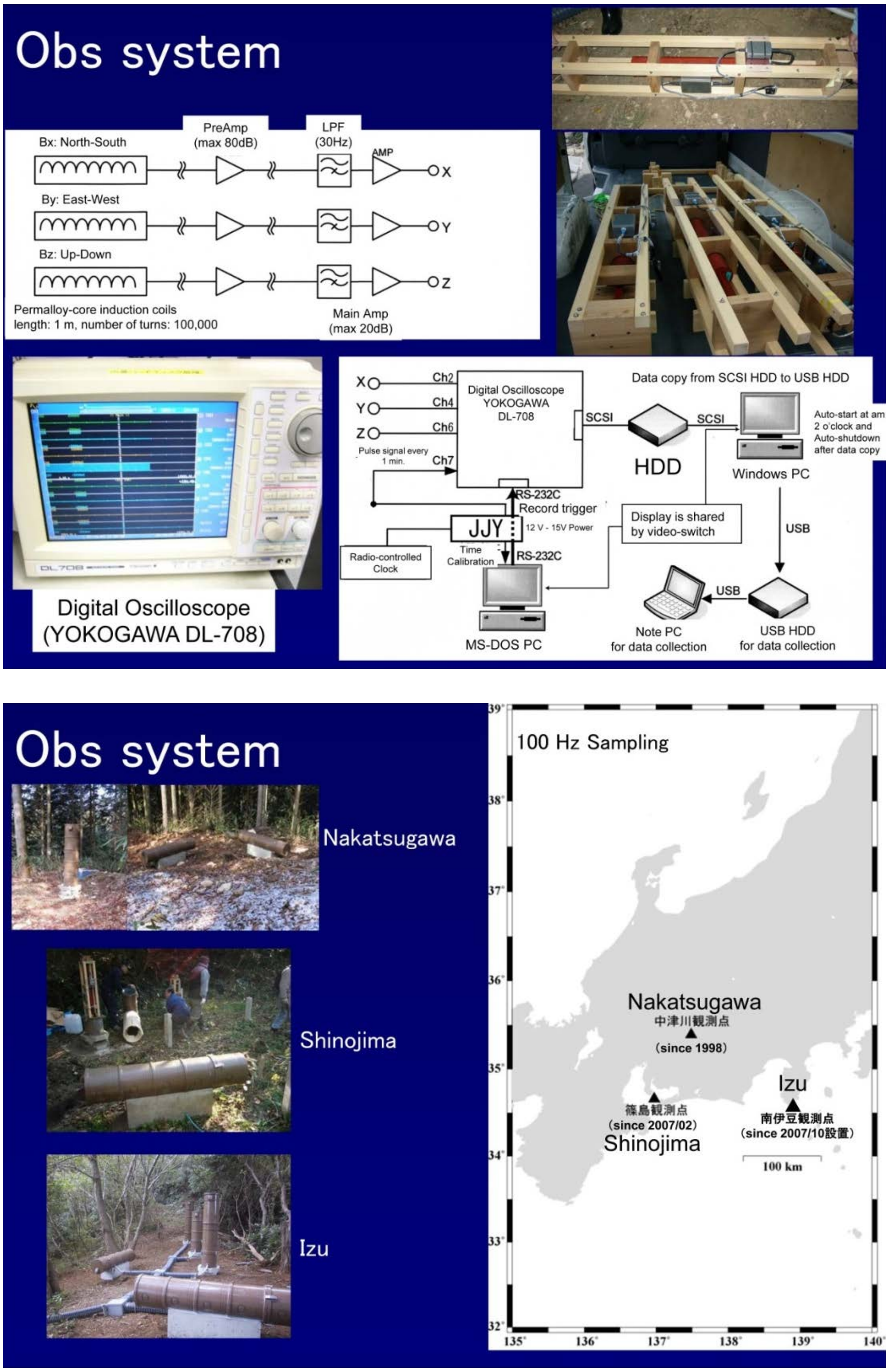

Figure 2. (a) The SR receiving system and (b) photos of the field sites used in our measurements.

and coherently at all sites. The block diagram of ULF/ELF observation system is shown in Figure 2 [see Ohta et al., 2009; Hata et al., 2010].

As magnetic sensors, we have three orthogonal induction coils of 100,000 turns winded on the permalloy core of 1.2 m length. Three magnetic field components are recorded (B_x: north-south direction. B_y: east-west direction, and B_z: vertical direction). The detected signals are amplified by pre-amplifiers with maximum gain of 80 dB. Pre-amplifiers include the standard low-pass filters with the cut-off frequency of 37.5 Hz (8th-order Chebyshev filter). The signals are fed then to the three channel receivers having the gain of 20 dB. The receiver output is directed to the ADC with sampling frequency of 100 Hz. The ADC used in the records is the Digital Oscilloscope recorder (DL-708).

The signal analysis is based on the FFT algorithm with the data length of 1024, so that the temporal resolution is about 10 s and relevant frequency resolution is about 0.1 Hz. Individual power spectra corresponding to the records of 10 s duration are averaged with no temporal overlap (the Bartlett's method). The ensemble of experimental data is formed by the power spectra averaged over 6 h periods of night observations for each date. The particular mode of nocturnal records was conditioned by severe industrial interference, which excludes obtaining the SR records during other hours of a day.

The upper right panel of Figure 2a contains two photos of magnetic sensors in addition to the block diagrams of our receiving equipment. The upper photo shows the field sensors and the box of antenna pre-amplifiers placed in the transportation cages. The lower left photo depicts the display of a digital oscilloscope used as the ADC in the measurement process.

The lower panel of Figure 2b contains two frames. The left frame demonstrates three photos showing the magnetic antennas positioned at each field site. The antennas are firmly fixed inside the secure plastic tubes covering the sensors. The right frame depicts the map of Japan with the positions of ULF/ELF observatories. The site names and the corresponding years of initiation of SR measurements are shown in the map.

4. Original experimental data

Figure 3 shows the experimental data relevant to two EQs that occurred in Japan in February and March of 2021. The figure contains four panels, in which the abscissa axis depicts the frequency (in Hz) range of the SR band and the ordinate shows the power spectra of the horizontal magnetic field components. The upper plots (Figures 3a and 3b) illustrate the power spectra of B_{WE} field component in February and March, while the lower plots (Figures 3c and 3d) show the spectra of B_{SN} field in February and March.

The power spectra were recorded for each date and averaged over the local night time interval from 16 to 20 h UT, i.e., when the industrial interferences were reduced. Thus, the one-day observations are shown in Figure 3 by a single SR curve. Each panel contains 20 power spectra corresponding to dates prior to and subsequent to the day of the EQ main shock. One may observe that the spectra in Figure 3 are of high quality. Each of them has a rather smooth outline and contains three distinct peaks corresponding to SR modes. The narrow band man-made interference is present occasionally in some records of B_{SN} field component at frequencies of a few Hz and below. Fortunately, this kind of remnants of interference does not affect the SR pattern.

SR oscillations are of higher intensity in the B_{SN} field component by a factor of ~2. The spectral pattern and relative intensity of field components indicate that the lightning sources were predominantly concentrated in the Central Africa and the South America global thunderstorm centers, as seen from the model data presented below. Such positioning of global thunderstorm activity agrees with the night time in Japan: the highest lightning activity is found in the equatorial Africa and in the Amazon basin for the particular time of day and particular season of observations [Nickolaenko and Hayakawa, 2002, 2014]. No unusual local thunderstorm activity was noted in February and March 2021.

One may observe reasonable closeness of all curves in Fig. 3 showing the daily averaged spectra. Still, there are several dates having noticeable departures from the bulk of 'regular' SR spectra. Deviations toward the higher power may reach a factor of two. One may also note a few reductions in the SR signals during particular days. We do not show the particular dates near the individual spectra for avoiding overloading with Figure 3. The necessary dates will be shown when comparing the model data with observations.

Figure 4 demonstrates day after day changes of integrated SR intensity recoded around the dates of two EQs that occurred in February (a) and March (b) of 2021. The EQ days are marked in the plots by downward vertical arrows, and the abscissa axes depict the date in February and March. The SR field power is shown along the ordinate. The daily power spectra that were shown in Fig. 3 were integrated in Fig. 4 in the frequency band from 4 to 23 Hz in both the B_{WE} (green lines) and B_{SN} (red lines) components. This operation provided the cumulative SR intensity observed during a particular day of observations. The black lines in Figure 4 depict alterations of cumulative magnetic field power of SR being the following sum: $|B|^2 = |B_{WE}|^2 + |B_{SN}|^2$.

The integrated SR power spectra allow us to estimate the cumulative intensity of ELF field for each day of observations. The patterns in Figure 4 have much in common, though noticeable departures might be observed for different months of observations. The major common feature of particular records is the absence of an abrupt increase in the records during the EQ major shock. Such behavior seems odd at the first glance, since everyone

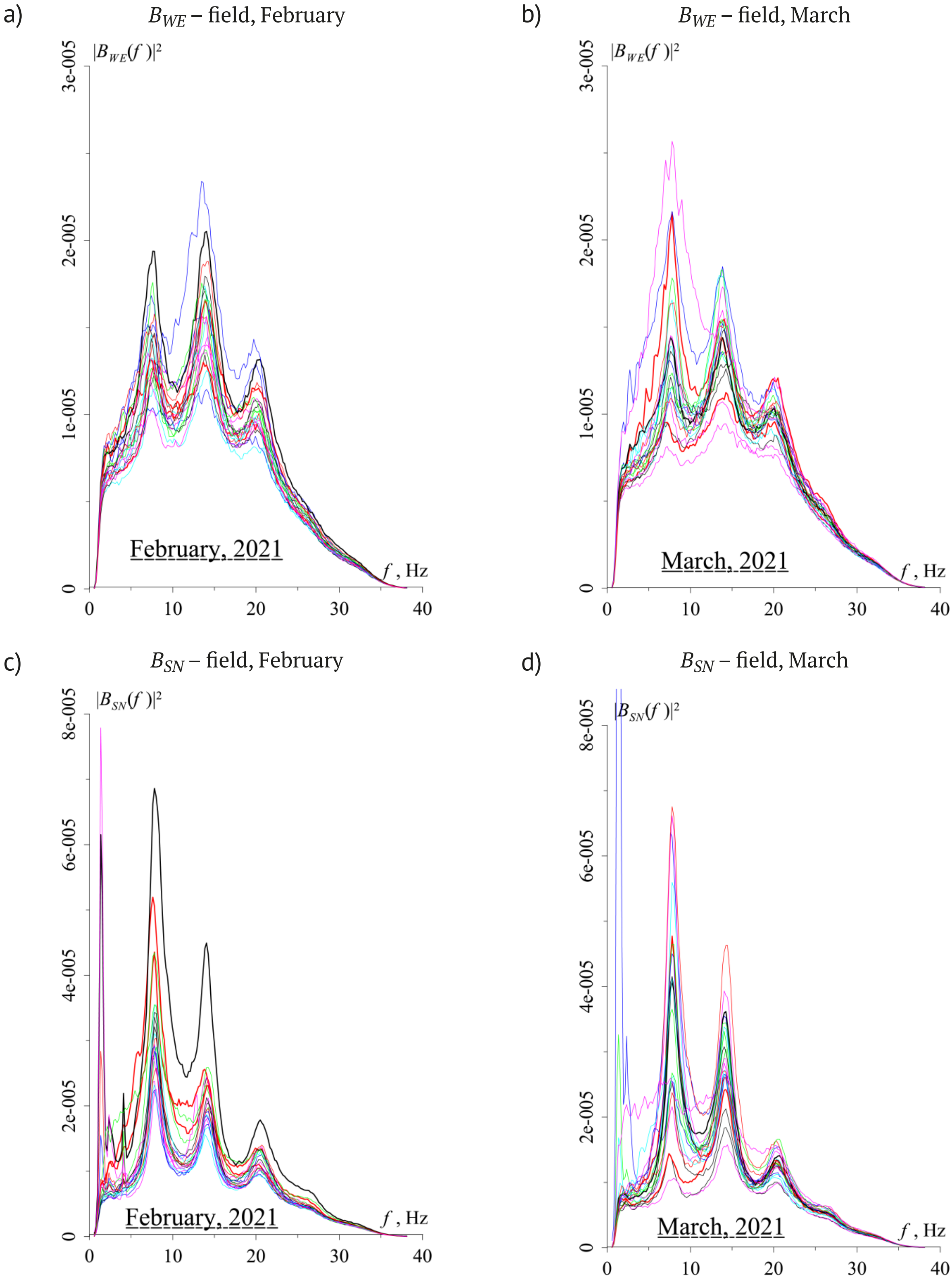

Figure 3. Survey of the recorded power spectra. (a) and (b) refer to B_{WE} in February and March, while (c) and (d) refer to B_{SN} in February and March, 2021.

understands that an EQ drives antenna mechanical vibrations, which occur in the static geomagnetic field and therefore drive enormous ELF signals. Fortunately, these signals were not recorded and could not affect the records since the EQs took place when the receiving equipment was switched off for avoiding the huge local industrial interference.

a)

b)

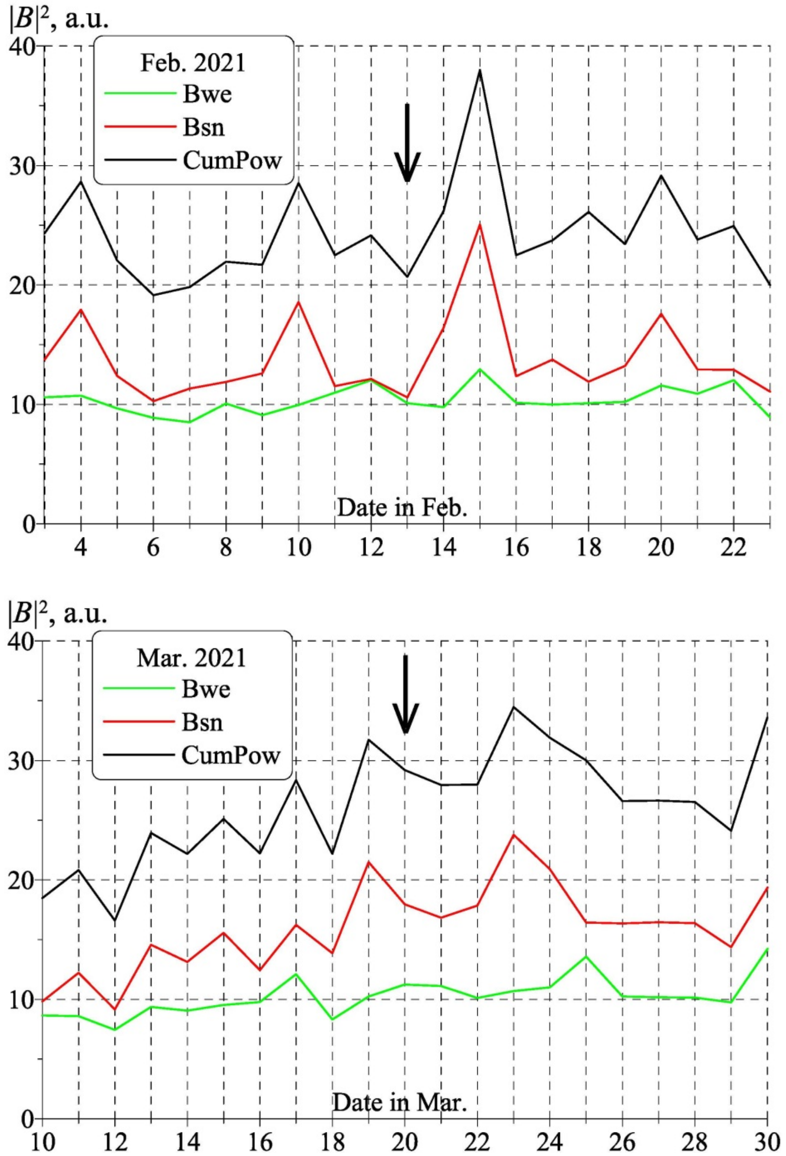

Figure 4. Temporal changes of cumulative SR power (black curves, CumPow) around the date of EQs (indicated by downward arrows) in February (a) and March (b) in 2021.

5. Model of seismogenic modifications in the lower ionosphere

If we think of the EQ hypocenter as the zone where tectonic stress is accumulated, then we can expect different seismogenic perturbations in the atmosphere and ionosphere above the EQ epicenter. Even though Fidani [2006] suggested an alternative interpretation to our initial SR anomaly [Hayakawa et al., 2005], we assume that anomalous signals in the SR band may originate following our previous works [Hayakawa et al., 2005; Nickolaenko et al., 2006; Hayakawa et al., 2020a]. An EQ of magnitude M_{EQ} reduces or increases the ionospheric height above the EQ zone. The horizontal distribution of our ionospheric non-uniformity is exactly the same as in our previous publications [Hayakawa et al., 2020a]: the radial Gaussian function of the scale depending on the EQ magnitude.

$$h_L(r) = \Delta h \exp\left(-\frac{r^2}{\rho_{EQ}^2}\right) \tag{1}$$

Here, $h_L(r)$ is the magnetic characteristic height at the distance r from the EQ epicenter, and Δh is the maximum modification positioned over the EQ center. And ρ_{EQ} is the radial scale radius.

The magnetic h_L and the electric h_C characteristic heights of the ionosphere [Nickolaenko and Hayakawa, 2002] are computed for the particular conductivity profile of atmosphere by using the full-wave solution in the form of Riccati equation [Galuk et al., 2019, 2020]. The regular profiles of conductivity are used far away from the EQ center. The maximally disturbed profile is used over the EQ epicenter, and here the maximum height modification Δh is computed. The radial variations of the characteristic height within the seismic non-uniformity are found from Eq. (1). The scale radius ρ_{EQ} of the non-uniformity (in km) is a function of the EQ magnitude M_{EQ}: $\rho_{EQ} = \exp(M_{EQ})$ [Ruzhin and Depueva, 1996]. In particular, $\rho_{EQ} = 1096.9$ km for the $M_{EQ} = 7$.

The "vertical modification" of the regular conductivity profile is described by the "compression coefficient" K_C. We postulate that the height compression coefficient is equal to:

$$K_C(M_{EQ}) = \frac{100}{M_{EQ}^2} \tag{2}$$

In particular, for $M_{EQ} = 7$ we obtain $K_C \approx 2$. This means that the conductivity profile above the EQ epicenter of the $M_{EQ} = 7$ magnitude is obtained from the regular one plotted against the "compressed" ordinate axis, i.e., against the heights divided by the coefficient K_C.

Different model conductivity profiles above the EQ epicenter of $M_{EQ} = 7$ are shown in Figure 5. Here, the altitude above the ground surface is shown along the ordinate in km and the abscissa shows the logarithm of air conductivity. The regular profile is shown by the bold black line. The disturbed profiles are depicted by color lines. The red line with dots depicts the compressed profile with $K_C = 2$.

If we elevate the lower ionosphere instead of reducing it, we should use the "expansion" coefficient as follows:

$$K_E(M_{EQ}) = 0.1786 \cdot M_{EQ} \tag{3}$$

The violet line with asterisks in Figure 5 indicates the "expanded" profile corresponding to $K_E \approx 1.25$. It is easy to see that these disturbed profiles are simply the regular ones "compressed" or "expanded" vertically.

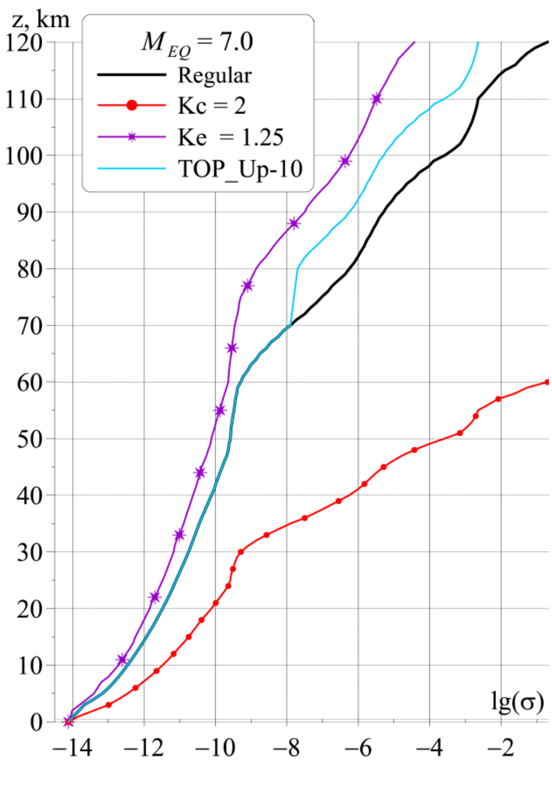

Figure 5. Vertical profiles of atmosphere conductivity: regular and disturbed (compression and expansion).

The thin blue line shows an additional model non-uniformity in Figure 5. This is the "TOP UP" disturbed profile as suggested by Hayakawa et al. [2020a]. It was obtained by the 10 km upward shift of the regular profile above the altitude of 70 km.

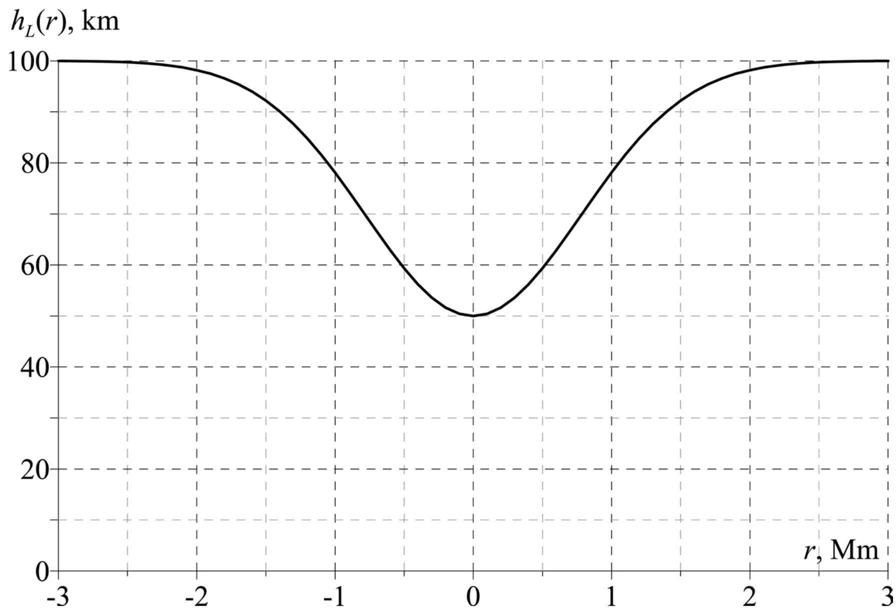

Figure 6. Line of equal conductivity when passing above the EQ epicenter ($r = 0$) for the "compression" model of $K_C = 2$ type.

Figure 6 shows the cross-section of seismogenic height modification in conductivity profile described by Eq. (1). The "compression" ionospheric modification is shown. The line in this figure depicts the height of a constant conductivity along the line crossing the EQ epicenter. We have chosen the constant corresponding to the undisturbed conductivity at the 100 km altitude, and it is equal to $\sigma_C = 2.63 \times 10^{-4}$ S/m [$\log(\sigma_C) = -3.58$]. The abscissa shows the radial horizontal distance from the epicenter ($r = 0$), and the ordinate depicts the altitude in km. The plot demonstrates the reduction of the local ionosphere height to 50 km just above the EQ center, while it was initially equal to the undisturbed 100 km (profile of compression). Since the observer distance in the experiment was about 1 Mm from the epicenters for both the EQs of $M_{EQ} \approx 7$ (the actual epicenter – observer distances were 1480 km in February and 990 km in March), we conclude that the disturbed height may reach ~82 km above the observatory. Hence, the power of SR signal might increase by a factor of $(100/82)^2 = 1.5$. This is a simple estimate of expected seismogenic effect, and the realistic modifications of resonance spectra will be shown below based on the computations using the 2D (two dimensional) telegraph equation (2DTE) algorithm [Galuk et al., 2019, 2020].

6. Results of model computations

We computed the regular and disturbed characteristic heights by using the full-wave solution in the form of Riccati equation [Galuk et al., 2019, 2020]. These complex electric and magnetic heights $h_C(f)$ and $h_L(f)$ [Nickolaenko and Hayakawa, 2002] which are essential in ELF wave propagation, were obtained for frequencies varying from 4 to 24 Hz with a step of 0.2 Hz.

Then, the characteristic heights were substituted into the 2DTE [Nickolaenko et al., 2006; Nickolaenko and Hayakawa, 2013; Galuk et al., 2019, 2020]. These equations account for the coordinates of the EQ epicenter, coordinates of the observer, and the position of a particular field source (Asia, Africa, or America). The solutions of electromagnetic problem were constructed for the regular and for the non-uniform (or disturbed) cavities. In the uniform cavity, the ionosphere is stratified, and the heights are independent of the angular coordinates θ and φ of the spherical coordinate system with the origin at the Earth's center. In the presence of seismogenic disturbance these layer heights depend on the angular distance from the EQ epicenter. Power spectra were computed of three

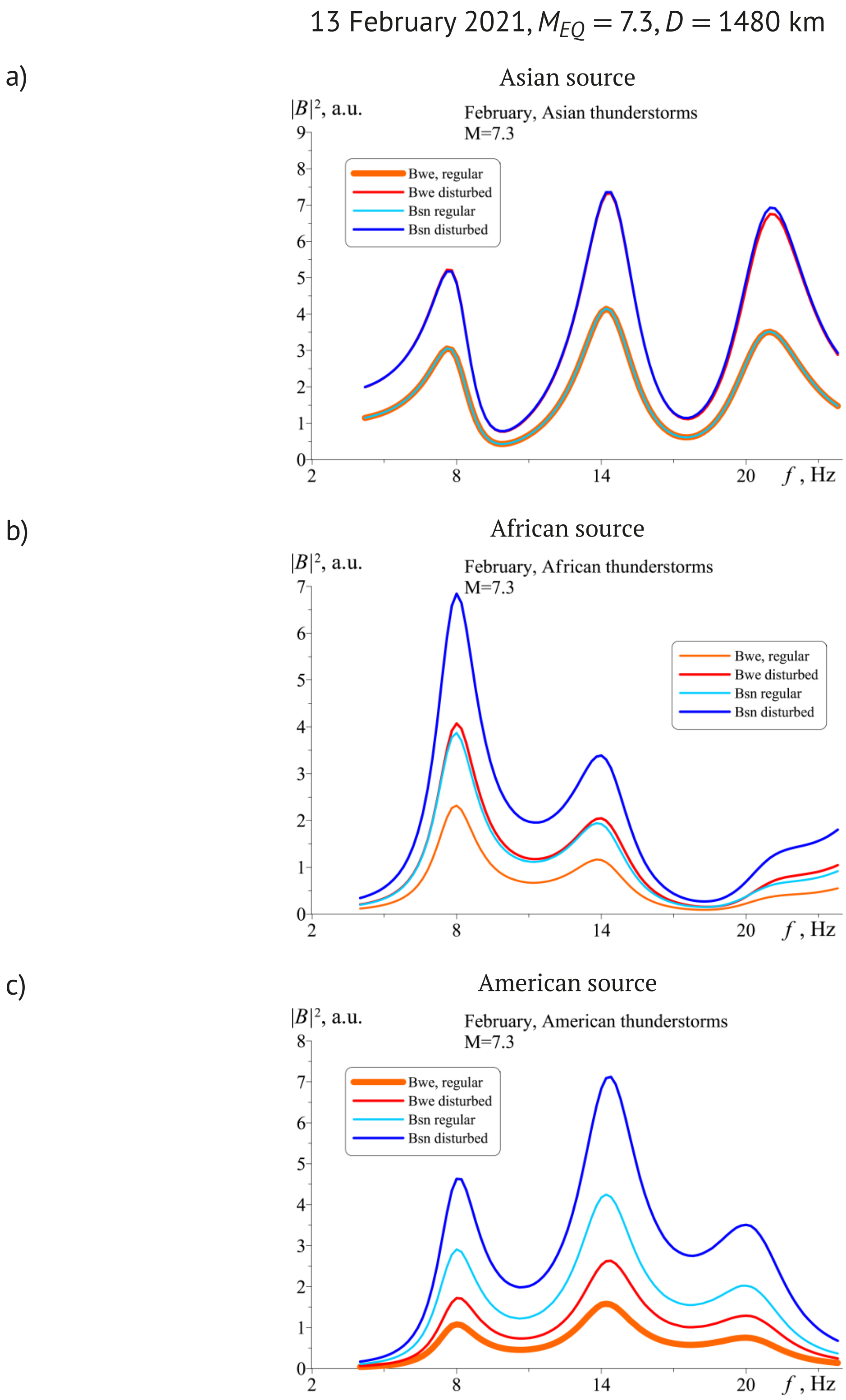

Figure 7. Simulated power spectra of SR observed in horizontal magnetic field components within the regular and disturbed Earth – ionosphere cavity when the source position is: in a – Asia; b – Africa; c – America. For the EQ on February 13, 2021.

field components: the vertical electric field $E(f)$ and two orthogonal horizontal magnetic fields $B_\varphi(f) = B_{WE}(f)$ and $B_\theta(f) = B_{SN}(f)$ defined in geography coordinate system. The results of computations are presented in Figs. 7 and 8.

Figures 7 and 8 depict the power spectra of SR computed for the horizontal magnetic fields $B_{WE}(f)$ and $B_{SN}(f)$. Computations were performed for the EQ for the presumed ionospheric modification that occurred on February 13, 2021 (Figure 7) and on March 20, 2021 (Figure 8). The bold lines refer to the spectra in the non-uniform (perturbed)

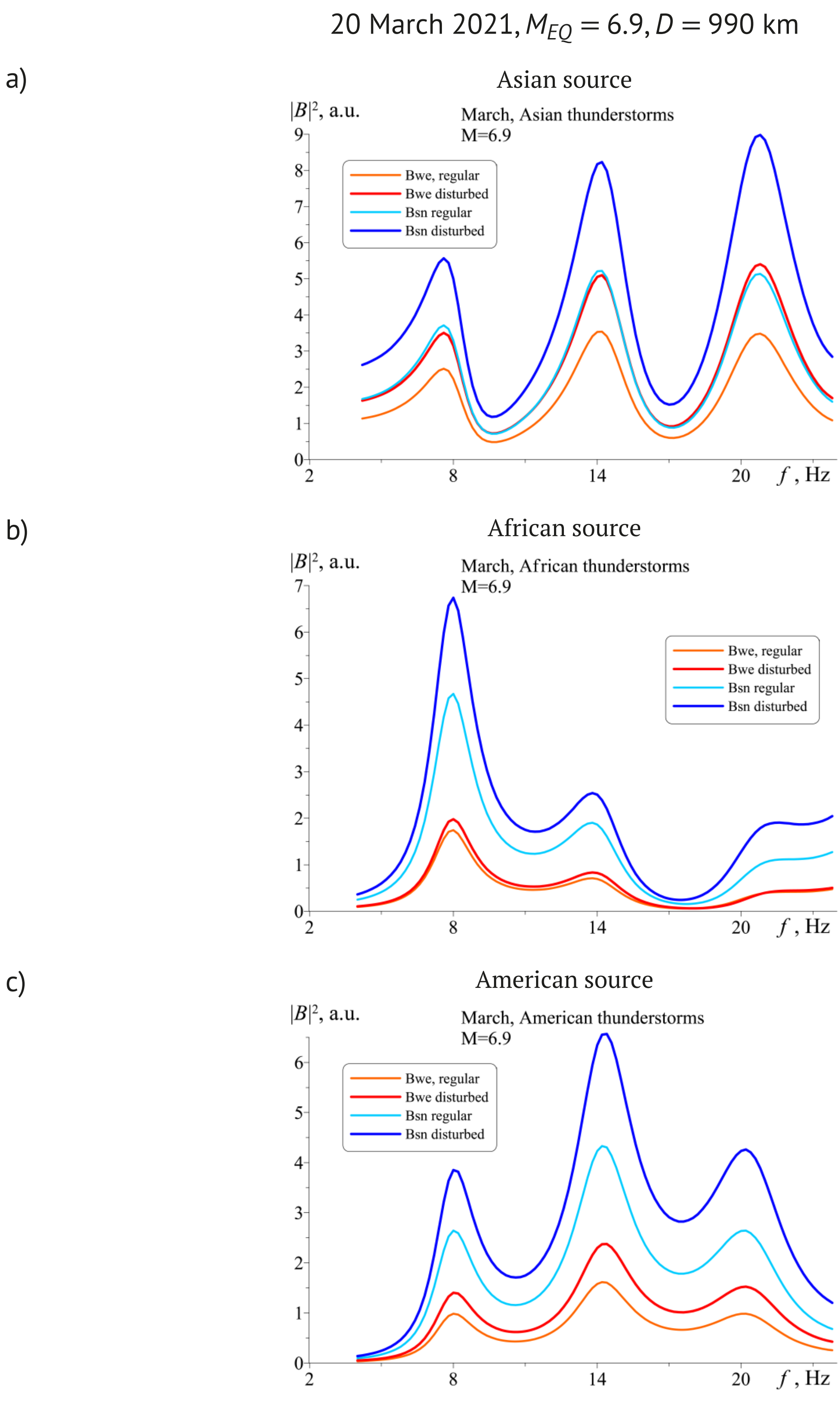

Figure 8. Simulated power spectra of SR observed in horizontal magnetic field components within the regular and disturbed Earth – ionosphere cavity when the source position is: in a – Asia; b – Africa; c – America. For the EQ on March 20, 2021.

cavity, while the thin lines depict data in the regular cavity. The observer is positioned at the SHI observatory (34.67° N, 137.01° E). The point field source is positioned at: a – Asia (10° N and 105° E); b – Africa (0° N and 25° E); or c – South America (0° N and 75° W). Plots in Fig. 7 correspond to the EQ in Japan on February 13, 2021 [14:07 UT; epicenter at (37.7 N, 141.7 E); $M_{EQ} = 7.3$] and plots in Fig. 8 demonstrate the model impact on the SR spectra of the second EQ on March 20, 2021 [09:09 UT; epicenter at (38.5° N, 141.6° E); $M_{EQ} = 6.9$].

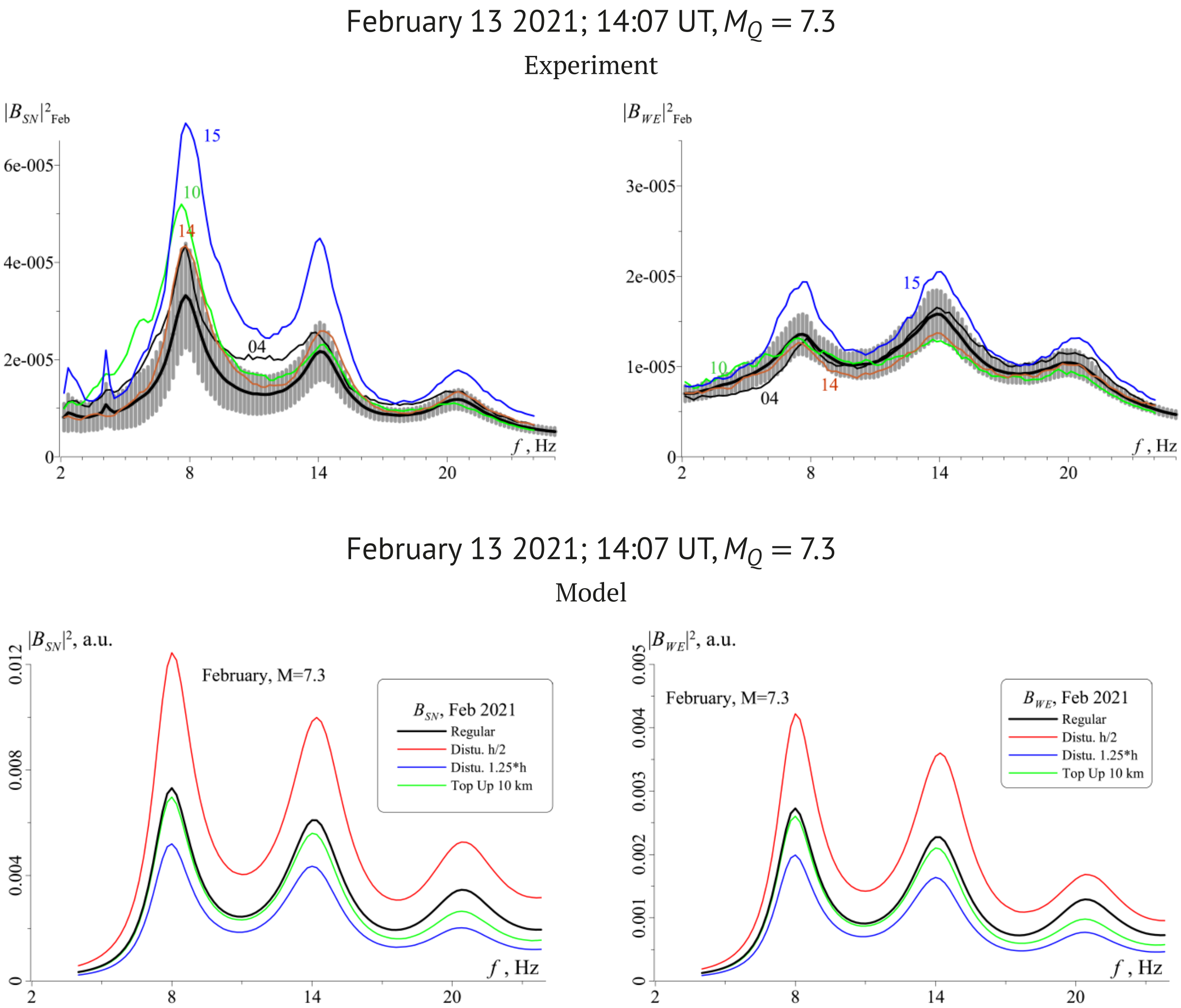

Figure 9. Comparison of experimental (upper row) and model (lower row) February spectra. In the upper row, the number next to each curve indicates the date of observation (e.g. 15 means the data for 15 February).

One may observe that the severe seismic disturbance in the ionosphere that we applied in the model is able to noticeably 'elevate' the SR power spectra over the frequency axis. The general outline of resonance curves noticeably depends on the position of the field source. These distinctions might be expected since the SR pattern varies with the source–observer distance [Nickolaenko and Hayakawa, 2002]. We will observe in what follows that the experimentally observed outline of power spectra corresponds to two field sources positioned in the equatorial Africa and in the South America (the Amazon Basin). We will not compare observations with the model spectra obtained for the Asian thunderstorms. Indeed, these thunderstorms are positioned at short distance from the field sites, however, the night time observations in Japan correspond to the minimum thunderstorm activity at this center.

We show in Figures 9 and 10 the reasonable correspondence among the observed and model spectra. Plots in the upper columns of these figures contain the experimental data observed in the B_{SN} and B_{WE} field components during February 2021 (Figure 9) and March 2021 (Figure 10). The experimental data are characterized by the average spectra and their standard deviation found over the whole period of observations. The average spectra are shown by the bold black lines, while the relevant standard deviations are outlined by the grey area. The thin color lines in the upper panels refer to individual spectra, and the dates are printed near the most deviating curves. Spectra of the B_{SN} field component are shown in the left frames of each figure and spectra of the B_{WE} field component are shown in the right column of plots. Experimental spectra are shown similarly in both figures. All the information (mean and standard deviation) is shown in the figures to demonstrate that anomalous signals go beyond the standard deviation criterion. We do not study the local lightning distribution around Japan, and we do not pursue the statistical distribution of SR spectra in this paper.

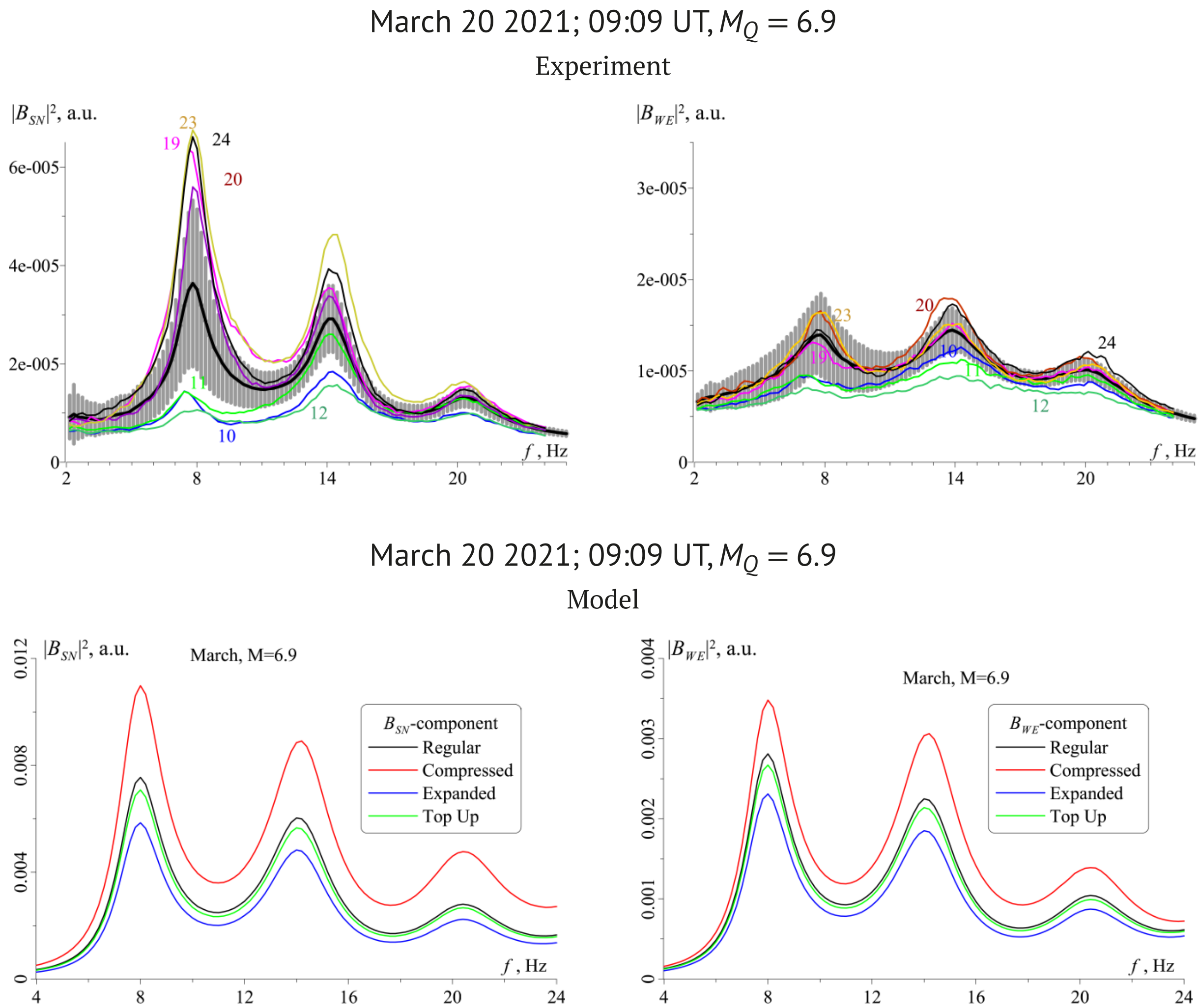

Figure 10. The same as Fig. 9, but for the March event. Comparison of experimental (upper row) and model (lower row) March spectra.

The model spectra are depicted below the experimental data to facilitate their comparison. Computations were performed for the B_{SN} and B_{WE} field components. Model data show the power spectra both in the uniform and non-uniform Earth–ionosphere cavities when the global thunderstorm activity is equally shared by the African (0° N and 25° E) and the American (0° N and 80° W) centers. Such a model corresponds to the time interval of observations from 16 to 20 h UT [Nickolaenko and Hayakawa, 2002, 2014].

One may observe that model computations provide the SR spectral pattern similar to that observed experimentally. Of course, some definite departures are present, which might be attributed to a rather simplified model of the unknown source distribution over the globe.

Different model spectra are shown in the lower frames in Figures 9 and 10. These spectra correspond to various kinds of ionospheric perturbations. The red lines depict power spectra in the presence of the “compressed” profiles with the parameter $K_C = 2$. The blue lines correspond to the “expanded” profiles with $K_E = 1.25$. The impact of the “Top Up” disturbance is shown by green lines.

By comparing the model and observed spectra of Figures 9 and 10 we observe the similarity in general outline of resonance curves: the ratio of modal power reduces with the mode number in approximately equal proportion both in the experiment and in the model. Such behavior arises from simultaneous “work” of two global thunderstorms positioned at different sides of the Atlantic Ocean. Application of two thunderstorm centers improved correspondence of the model to experimental data in comparison with Hayakawa et al. [2021b].

The obvious feature of model results is that the downward “compression” of the conductivity profile noticeably elevates the power spectra of SR above the regular spectrum. In contrast, the disturbances of “expanded” type or of the “Top Up” type shift the resonance spectra downward, to lower values of spectral density.

7. Discussion

Processing of observational data on SR for two EQs in the spring of 2021 and comparisons of observational results with the model computations allow us to conclude that the seismogenic perturbations were really generated before and these EQs. The spectral modifications preceding EQs might be attributed to the both types of ionospheric perturbations (compressed and expanded), while the noticeable disturbances following the first major main shock are predominantly of the "compressed" type.

As stated in Introduction, a few hypotheses have been proposed, but the major two are (1) chemical channel, in which the emanation of radon and radioactive gases plays a crucial role in disturbing the conductivity of the atmosphere, thereby leading to the ionospheric perturbation [Pulinets and Boyarchek, 2004], and (2) AGW hypothesis, in which AGWs are excited above the EQ epicenter and propagating upwards, resulting in the perturbation in the ionosphere [Hayakawa, 2009, 2013; Molchanov and Hayakawa, 2008; Hayakawa, 2015]. Based only on the comparison of observational results with theoretical studies in this paper, it is rather difficult for us to suggest which hypothesis is more appropriate than the other for our present case. However, there has been accumulated a lot of evidence on the AGW hypothesis [Miyake et al., 2002; Shvets et al., 2004; Rozhnoi et al., 2013; Yang et al., 2019, 2020; Yang and Hayakawa, 2020; Lizunov et al., 2020; Carbone et al., 2021; Chen et al., 2021; Kundu et al., 2022], so we try to interpret our observational results on SR with the use of this AGW hypothesis. So, the profile "compression" might be explained in the following way. The sub-surface process during the EQ preparation phase before an EQ is expected to induce Earth's surface deformation, or ground trembling [Kamiyama et al., 2014; Yang et al., 2020; Chen et al., 2020a, b]. These Earth's surface vibrations are dominant in the frequency of AGWs, generate the internal gravity waves in the atmosphere (or AGWs) propagating from the future epicenter. The propagating AGWs gradually reach the higher strata of atmosphere. Their amplitude increases with altitude owing to reduction in the atmosphere density with height [Lizunov et al., 2020]. Around the heights of 60-100 km, the AGWs gain the amplitude which is able to noticeably move the lower ionosphere edge upward or downward. These upward and downward displacements are linked to the non-linear process causing the disturbances in the conducting layers of mesosphere. The ionospheric non-uniformities of both types can emerge as a result that are observed as modulations in the level of SR prior to the EQ main shock.

During the EQ main shock and aftershocks, the AGW amplitude substantially increases, and these waves reach the "threshold" amplitude in the lower strata, which allows them to launch the non-linear processes increasing the air conductivity just above the stratosphere heights. As a result, the "compression" occurs of the poorly conducting strata, the ionosphere "goes down" in the EQ vicinity, and the SR amplitude increases at moderate distances from the EQ epicenter after the main shock.

It follows from the SR records that most probably the first major EQ in February 2021 was associated with the "compression" type of disturbance, since the pronounced elevations (precursors) were observed on February 04 and 10. The same is valid for the ionospheric modifications after the main shock on February 14 and 15. In contrast, the subsequent EQ in March was associated with the modifications of both types. The precursory anomalies in SR spectra on March 10, 11, and 12 might be associated with the "expansion" modifications, which elevate the lower ionosphere boundary. Anomalies on March 19 (precursor) and on March 20, 23, 24 (successors) should be attributed to the "compression" type of disturbance when the gap between the ground and the lower edge of the ionosphere is reduced.

The above conclusions are supported in the clearest way by the records of B_{NS} field component having greater amplitude. The behavior of the smaller B_{WE} component is not so explicit (univalent). In fact, modulations in the smaller B_{NS} – component of the field sometimes noticeably deviate from the more pronounced B_{WE} – field modulations.

References

Carbone, V., M. Piersanti, M. Materossi, R. Battiston, F. Lepreti and P. Ubertini (2021). A mathematical model of lithosphere-atmosphere-ionosphere coupling of seismic events, Sci. Rep., 11, 8682, https://doi.org/10.1038/s41598-021-88125-7

Chen, C.H., L.C. Lin, T.K. Yeh, S. Wen, H. Yu, C. Yu, Y. Gao, P. Han, Y.Y. Sun, J.Y. Liu, H. Lin, C.C. Tang, C.M. Lin, H.H. Hsieh and P.J. Lu (2020a). Determination of epicenters before earthquakes utilizing far seismic and GNSS data: Insights from ground vibrations, Remote Sensing, 12, 3252, doi:10.3390/rs12193252

Chen, C.H., Y.Y. Sun, S. Wen, P. Han, L.C. Lin, H. Yu, X. Zhang, Y. Gao, C.C.Tang, C.H. Lin and J.Y. Liu (2020b). Spatiotemporal changes of seismicity rate during earthquakes, Natural Hazards Earth System Sci., 20, 3333-3341, https://doi.org/10.5194/nhess-20-3333-2020

Chen, C.H., Y.Y. Sun, K. Lin, J. Liu, Y. Wang, Y. Gao, D. Zhang, R. Xu and C. Chen (2021). The LAIC coupling associated with the M6 Luxian earthquake in China on 16 September 2021, Atmosphere, 12, 1621, https://doi.org/10.1541/jae.30.103.

Christofilakis, V., E.G. Tatsis, C. Votis, I. Contopoulos, C. Repapis and V. Tritakis (2019). Significant ELF perturbations in the Schumann resonance band before and during a shallow mid-magnitude seismic activity in the Greek area (Kalpuki), J. Atmos. Solar-terr. Phys., 182, 138-146.

Conti, L., P. Picozza and A. Sotgiu (2021). A critical review of ground based observations of earthquake precursors, Front. Earth Sci., 9, 676766, https://doi.org/10.3389/feart.2021.676766

De Santis, A., C. Abbattista, L. Alfonsi, L. Amoruso, S.A. Campuzano, M. Carbone, C. Cesaroni, G. Cianchini, R. Di Giovambattista, D. Marchetti, L. Martino, L. Perrone, A. Piscini, M.L. Rainone, M. Sodani, L. Spogli and F. Santoro (2019). Geosystems view of earthquakes, Entropy, 21, 4, 412, doi:10.3390/e21040412

Fidani, C. (2006). On electromagnetic precursors of earthquakes: Model and instruments, IPHW (Intl Project Hessdalen Workshop), Medicina, Italy, June 2006, 25-41.

Figueredo, P.S., B.M. Ortega, M. Pazos, D.R. Osorio, E.A. Mascote, V.M. Mendosa and R. Garduno (2021). Schumann resonance anomalies possibly associated with large earthquakes in Mexico, Indian J. Physics, 95, 1959-1966, https://doi.org/10.1007/s12648-020-01865-6

Florios, K., I. Contopoulos, G. Tatsis, V. Christofilakis, S. Chronopoulos, C. Repapis, and V. Tritakis (2021). Possible earthquake forecasting in a narrow space-time-magnitude window, Earth Sci. Informatics, 14, 349-364, https://doi.org/10.1007/s12145-020-00535-9

Freund, F. (2013). Earthquake warning – A multidisciplimary challenge from the ground up to space, Acta Geophys., 61, 775-807.

Galuk, Yu.P., I.G. Kudintseva, A.P. Nickolaenko and M. Hayakawa (2019). Scattering of ELF radio waves by a localized non-uniformity in the lower ionosphere, J. Atmos. Solar-terr. Phys., 194, 105093.

Galuk, Yu.P., I.G. Kudintseva, A.P. Nickolaenko and M. Hayakawa (2020). Modifications of Schumann resonance spectra as an estimate of causative earthquake magnitude: the model treatment, J. Atmos. Solar-terr. Phys., 194, 209, 105392, https://doi.org/10.1016/j.jastp.2020.105392

Gazquez, J.A., R.M. Garcia, N.N. Castellano, M.R. Fernandez-Ros, A.J. Perea-Moreno and F. Manzano-Agugliaro (2017). Applied engineering using Schumann resonance for earthquake prediction, Appl. Sci., 7, 1113, doi:10.3390/app7111113

Hata, M., K. Ohta, J. Izutsu, I. Takumi, T. Sato, S. Yahashi and N. Watanabe (2010). Development of ULF band receiver for detecting electromagnetic-wave precursor of earthquakes, J. Atmos. Electr., 30, 13-36 (in Japanese).

Hayakawa, M. (2015). Earthquake Prediction with Radio Techniques, John Wiley & Sons, Singapore, 294.

Hayakawa, M. (Ed) (2009). Electromagnetic Phenomena Associated with Earthquakes, Transworld Research Network, Trivandrum, India, 279.

Hayakawa, M. (Ed) (2013). Earthquake Prediction Studies: Seismo Electromagnetics, TERRAPUB Tokyo, 279.

Hayakawa, M., K. Ohta, A.P. Nickolaenko and Y. Ando (2005). Anomalous effect in Schumann resonance phenomena observed in Japan, possibly associated with the Chi-chi earthquake in Taiwan, Ann. Geophysicae, 23, 1335-1346.

Hayakawa, M., Y. Hobara, K. Ohta and K. Hattori (2011). The ultra-low-frequency magnetic disturbances associated with earthquakes, Earthq. Sci., 24, 523-534.

Hayakawa, M., A. Schekotov, J. Izutsu and A.P. Nickolaenko (2019). Seismogenic effects in ULF/ELF/VLF electromagnetic waves, Int. J. Electronics Appl. Res. (IJEAR), 6, 2, 1-86, doi:10.4236/ojer.2023.123003, ISSN 2395-0064

Hayakawa, M., A.P. Nickolaenko, Y.P. Galuk and I.G. Kudintseva (2020a). Scattering of extremely low frequency electromagnetic waves by a localized seismogenic ionospheric perturbation: Observation and interpretation, Radio Sci., 55, e2020RS007130, https://doi.org/10.1029/2020RS007130

Hayakawa, M., Y. Kasahara, T. Nakamura, F. Muto, T. Horie, S. Maekawa, Y. Hobara, A.A. Rozhnoi, M. Solovieva and O.A. Molchanov (2010). A statistical study on the correlation between lower ionospheric perturbations as seen by subionospheric VLF/LF propagation and earthquakes, J. Geophys. Res., 115, A09305, doi:10.1029/2009JA015143

Hayakawa, M., J. Izutsu, A. Schekotov, S.S. Yang, M. Solovieva and E. Budilova (2021a). Lithosphere-atmosphere-ionosphere coupling effects based on multiparameter precursors observations for February-March 2021 earthquakes (M~7) in the offshore of Tohoku area of Japan, Geosciences, 11, 481, https://doi.org/10.3390/geosciences11110481

Hayakawa M., J. Izutsu, A.Yu. Schekotov, A.P. Nickolaenko, Yu.P. Galuk, and I.G. Kudintseva (2021b). Anomalies of Schumann resonances as observed near Nagoya associated with two huge (M~7) Tohoku offshore earthquakes in 2021, J. Atmos. Solar-terr. Phys., 225 (Nov.2021), 105761, https://doi.org/10.1016/j.jastp.2021.105761

Kamiyama, M., M. Sugito, M. Kuse, A. Schekotov and M. Hayakawa (2014). On the precursors to the 2011 Tohoku earthquake: Crustal movements and electromagnetic signatures, Geomatics, Natural Hazards and Risk, doi:10.1080/19475705.2014.937773

Kundu, S., S. Chowdhury, S. Gosh, S. Sasmal, D. Politis, S.M. Potirakis, S.S. Yang, S.K. Chakhrabarti and M. Hayakawa (2022). Seismogenic anomalies in Atmospheric Gravity Waves as observed from SABER/TIMED satellites during large earthquakes, J. Sensors, 2022, 3201104, https://doi.org/10.1155/2022/3201104

Liu, J.Y., Y.I. Chen, Y.J. Chuo and C.S. Chen (2006). A statistical investigation of pre-earthquake ionospheric anomaly, J. Geophys. Res., 111, A05304, https://doi.org/10.1029/2005JA011333

Lizunov, G., T. Skorokhod, M. Hayakawa and V. Korepanov (2020). Formation of ionospheric precursors of earthquakes – Probable mechanism and its substantiation, Open J. Earthq. Res. (OJER), 9, 2, doi:10.4236/ojer.2020.92009

Maki, K. and T. Ogawa (1983). ELF emissions associated with earthquakes, J. Atmos. Electr., 3, 41-44.

Miyaki, K., M. Hayakawa and O.A. Molchanov (2002). The role of gravity waves in the lithosphere-ionosphere coupling as revealed from the subionospheric LF propagation data, in "Seismo Electromagnetics: Lithosphere-Atmosphere-Ionosphere Coupling, ed. by Hayakawa, M. and Molchanov, O.A., TERRAPUB, Tokyo, Japan, 229-232.

Molchanov, O.A. and M. Hayakawa (2008). Seismo Electromagnetics and Related Phenomena: History and latest results, TERRAPUB Tokyo, 189.

Molchanov, O., E. Fedorov, A. Schekotov, E. Gordeev, V. Chebrov, V. Surkov, A. Rozhnoi, S. Andreevsky, D. Iudin, S. Yunga, A. Lutikov, M. Hayakawa and P.F. Biagi (2004). Lithosphere-atmosphere-ionosphere coupling as governing mechanism for preseismic short-term events in atmosphere and ionosphere, Natural Hazards Earth System Sci., 4, 757-767.

Nickolaenko, A.P. and M. Hayakawa (2002). Resonances in the Earth-ionosphere Cavity, Kluwer Acad. Pub., Dordrecht, 389.

Nickolaenko, A.P. and M. Hayakawa (2013). Localized ionospheric disturbance over the earthquake center and modifications of Schumann resonance electromagnetic fields, Geomatics, Natural Hazards and Risk, 5, 3, 271-283.

Nickolaenko, A.P. and M. Hayakawa (2014). Schumann Resonances for Tyros: Essentials of Global Electromagnetic Resonances in the Earth-Ionosphere Cavity, Springer Tokyo, 348.

Nickolaenko, A.P., M. Hayakawa, M. Sekiguchi, Y. Ando and K. Ohta (2006). Model modifications in Schumann resonance intensity caused by a localized ionospheric disturbance over the earthquake epicenter, Ann. Geophysicae, 24, 567-575.

Nickolaenko, A.P., Yu.P. Galuk and M. Hayakawa (2016a). Vertical profile of atmospheric conductivity that matches Schumann resonance observations, SpringerPlus, 5, 106, https://doi.org/10.1186/s40064-016-1742-3

Nickolaenko, A.P., A.V. Shvets and M. Hayakawa (2016b). Propagation of extremely low-frequency radio waves, in Wiley Encyclopedia of Electric and Electronics Engineering, 1-20, https://doi.org/10.1002/047134608X.W1257.pub2

Ohta, K., N. Watanabe and M. Hayakawa (2006). Survey of anomalous Schumann resonance phenomena observed in Japan, in possible association with earthquakes in Taiwan, Phys. Chem. Earth, 31, 397-402.

Ohta, K., J. Izutsu and M. Hayakawa (2009). Anomalous excitation of Schumann resonances and additional anomalous resonances before the 2004 Mid-Niigata prefecture earthquake and the 2007 Noto Hantou earthquake, Physics and Chemistry of the Earth, Parts A/B/C, 34, 441-448, doi:10.1016/j.pce.2008.07.008

Ohta K., J. Izutsu, A. Schekotov and M. Hayakawa (2013). The ULF/ELF electromagnetic radiation before the 11 March 2011 Japanese earthquake, Radio Sci., 48, 587-596.

Picozza, P., L. Conti and A. Sotgiu (2021). Looking for earthquake precursors from space: A critical review, Front. Earth Sci., 9, 578, https://doi.org/10.3389/feart.2021.676775

Ouyang, X., X. Zhang, A.P. Nickolaenko, M. Hayakawa, X. Shen and Y. Miao (2013). Schumann resonance observation in China and anomalous disturbance possibly associated with Tohoku M9.0 earthquake, Earthq. Sci., 26, 2, 137-145.

Ouzounov, D., S. Pulinets, K. Hattori and P. Taylor (Eds) (2018). Pre-Earthquake Processes: A multidisciplinary approach to earthquake prediction studies, AGU monograph 234, Wiley, 365.

Pulinets, S.A. and K. Boyarchuk (2004). Ionospheric Precursors of Earthquakes, Springer Berlin, 315p.

Rozhnoi, A., M. Solovieva and M. Hayakawa (2013). VLF/LF signals method for searching of electromagnetic precursors, in "Earthquake Prediction Studies: Seismo Electromagnetics", ed. by M. Hayakawa, TERRAPUB, Tokyo, 31-48.

Ruzhin, Y.Y. and A.K. Depueva (1996). Seismoprecursors in space as plasma and wave anomalies, J. Atmos. Electr., 16, 3, 271-288.

Sasmal, S., S. Chowdhury, S. Kundu, D.Z. Politis, S.M. Potirakis, G. Balasis, M. Hayakawa and S.K. Chakrabarti (2021). Pre-seismic irregularities during the 2020 Samos (Greece) earthquake (M = 6.9) as investigated from multi-parameter approach by ground and satellite-based techniques, Atmosphere, 12, 1059., https://doi.org/10.3390/atmos12081059.

Schekotov, A., O. Molchanov, K. Hattori, E. Fedorov, V.A. Gladyshev, G.G. Belyaev, V. Chebrov, V. Sinitsin, E. Gordeev and M. Hayakawa (2006). Seismo-ionospheric depression of the ULF geomagnetic fluctuations at Kamchatka and Japan, Phys. Chem. Earth, 31, 313-318.

Schekotov, A.Y., O.A. Molchanov, M. Hayakawa, E.N. Fedorov, V.N. Chebrov, V.I. Sinitsin, E.F. Gordeev, G.G. Belyaev and N.V. Yagova (2007). ULF/ELF magnetic field variation from atmosphere by seismicity, Radio Sci., 42, RS6S90, doi:10.1029/2005RS003441

Schekotov, A. and M. Hayakawa (2017). ULF/ELF Electromagnetic Phenomena for Short-term Earthquake Prediction, LAP Lambert Academic Publishing, Beau Bassin, Mauritus, 102.

Schekotov, A., E. Fedorov, O.A. Molchanov and M. Hayakawa (2013). Low frequency electromagnetic precursors as a prospect for earthquake prediction, in "Earthquake Prediction Studies: Seismo Electromagnetics", Ed. by M. Hayakawa, TERRAPUB Tokyo, 81-99.

Shvets, A.V., M. Hayakawa, O.A. Molchanov and Y. Ando (2004). A study of the ionospheric response to regional seismic activity by VLF radio sounding, Phys. Chem Earth, 29, 627-637, https://doi.org/10.1016/j.pce.2003.08.063

Sorokin, V., V. Chmyrev and M. Hayakawa (2015). Electrodynamic Coupling of Lithosphere-Atmosphere-Ionosphere of the Earth, NOVA Sci. Pub. Inc., New York, USA, 355.

Sorokin, V.M., V.M. Chmyrev and M. Hayakawa (2020). A review on electrodynamic influence of atmospheric processes to the ionosphere, Open J. Earthq. Res. (OJER), 9, 2 doi:10.4236/ojer.2020.92008

Surkov, V. and M. Hayakawa (2014). Ultra and Extremely Low Frequency Electromagnetic Fields, Springer Tokyo, 486.

Tritakis, V., I. Contopoulos, J. Mlynarczyk, V. Christofilakis, G. Tatsis and C. Repapis (2022). How effective and prerequisite are extremely low frequency (ELF) recordings in the Schumann resonances band to function as seismic activity precursors, Atmosphere, 13, 185. https://doi.org/10.3390/atmos13020185

Welch, P.D. (1967). The use of Fast Fourier Transform for the estimation of power spectra: A method based on time averaging over short, modified periodograms, IEEE Trans. Audio & Electroacoustics, AU-15, 2, 70-73, doi:10.1109/TAU.1967.1161901

Yang, S.S., T. Asano and M. Hayakawa (2019). Abnormal gravity wave activity in the stratosphere prior to the 2016 Kumamoto earthquakes, J. Geophys. Res.: Space Physics, 124, 1410-1425, doi:10.1029/2018ja026002

Yang, S.S. and M. Hayakawa (2020). Gravity wave activity in the stratosphere before the 2011 Tohoku earthquake as the mechanism of lithosphere-atmosphere-ionosphere coupling, Entropy, 22, 110, doi:10.3390/e22010110

Yang, S.S., S.M. Potirakis, S. Sasmal and M. Hayakawa (2020). Natural time analysis of Global Navigation Satellite System surface deformation: The case of the 2016 Kumamoto earthquakes, Entropy, 22, 674, doi:10.3390/e22060674

Zhou, H., Z. Zhou, X. Qiao and H. Yu (2013). Anomalous phenomena in Schumann resonance band observed in China before the 2011 magnitude 9.0 Tohoku earthquake in Japan, J. Geophys. Res.: Atmospheres, 118, 23, 13.338, https://doi.org/10.1002/2013JD020269

***CORRESPONDING AUTHOR: Masashi HAYAKAWA**,
Hayakawa Institute of Seismo Electromagnetics Co. Ltd. (Hi-SEM), The University of Electro-Communications (UEC) Alliance Center
#521, 1-1-1 Kojima-cho, Chofu, 182-0026, Japan
e-mail: hayakawa@hi-seismo-em.jp